A&A 674, A98 (2023)
https://doi.org/10.1051/0004-6361/202346043

Astronomy & Astrophysics
Special issue

Solar Orbiter First Results (Nominal Mission Phase)

Clustering of magnetic reconnection exhausts in the solar wind: An automated detection study

Naïs Fargette[1,2], Benoît Lavraud[3,2], Alexis P. Rouillard[2], Pierre S. Houdayer[4], Tai D. Phan[5], Marit Øieroset[5], Jonathan P. Eastwood[1], Georgios Nicolaou[6], Andrei Fedorov[2], Philippe Louarn[2], Christopher J. Owen[6], and Tim S. Horbury[1]

[1] The Blackett Laboratory, Department of Physics, Imperial College, SW72AZ London, UK
e-mail: n.fargette@ic.ac.uk
[2] Institut de Recherche en Astrophysique et Planétologie, CNRS, UPS, CNES, 31400 Toulouse, France
[3] Laboratoire d'astrophysique de Bordeaux, Univ. Bordeaux, CNRS, 33600 Pessac, France
[4] LESIA, Observatoire de Paris, CNRS, 92190 Meudon, France
[5] Space Sciences Laboratory, University of California, Berkeley, CA 94720, USA
[6] Mullard Space Science Laboratory, University College London, Dorking, Surrey RH56NT, UK

Received 31 January 2023 / Accepted 20 April 2023

ABSTRACT

Context. Magnetic reconnection is a fundamental process in astrophysical plasmas that enables the dissipation of magnetic energy at kinetic scales. Detecting this process in situ is therefore key to furthering our understanding of energy conversion in space plasmas. However, reconnection jets typically scale from seconds to minutes in situ, and as such, finding them in the decades of data provided by solar wind missions since the beginning of the space era is an onerous task.
Aims. In this work, we present a new approach for automatically identifying reconnection exhausts in situ in the solar wind. We apply the algorithm to Solar Orbiter data obtained while the spacecraft was positioned at between 0.6 and 0.8 AU and perform a statistical study on the jets we detect.
Methods. The method for automatic detection is inspired by the visual identification process and strongly relies on the Walén relation. It is enhanced through the use of Bayesian inference and physical considerations to detect reconnection jets with a consistent approach.
Results. Applying the detection algorithm to one month of Solar Orbiter data near 0.7 AU, we find an occurrence rate of seven jets per day, which is significantly higher than in previous studies performed at 1 AU. We show that they tend to cluster in the solar wind and are less likely to occur in the tenuous solar wind ($<10\,\mathrm{cm}^{-3}$ near 0.7 AU). We discuss why the source and the degree of Alfvénicity of the solar wind might have an impact on magnetic reconnection occurrence.
Conclusions. By providing a tool to quickly identify potential magnetic reconnection exhausts in situ, we pave the way for broader statistical studies on magnetic reconnection in diverse plasma environments.

Key words. magnetic reconnection – plasmas – solar wind – methods: data analysis

1. Introduction

Magnetic reconnection is a fundamental energy-transfer process triggered at kinetic scales in plasmas, that converts magnetic energy into kinetic and thermal energy while allowing a global reconfiguration of the magnetic field topology. The typical magnetic field configuration of a reconnection site is shown in Fig. 1, with a plasma exhaust bounded by two discontinuities that are akin to rotational discontinuities (Gosling et al. 2005a). A spacecraft crossing a reconnection exhaust would observe an ion jet as well as an electron jet, both coincidental with a sharp rotation in the magnetic field and an electric current. Additional signatures may also arise, such as a decrease in the magnetic field strength owing to energy conversion, an increase in electron temperature, as well as an increase in density (e.g., Gosling et al. 2005a, Paschmann et al. 2013). In order to best identify the reconnection signatures in the magnetic field and velocity, the *lmn* coordinate system associated with the magnetic field rotation is usually used (Sonnerup & Cahill 1967), where l is the maximum variance direction of the magnetic field, n is its minimum variance direction (normal to the current sheet), and m is the direction completing the frame. The reconnection jet would then align with the l direction, making it easy to detect and characterise.

To test whether a plasma jet is indeed consistent with a rotational discontinuity, and thus possibly the result of reconnection, a test of the Walén relation is often performed. The Walén relation is derived from jump properties for an Alfvénic rotational discontinuity (Hudson 1970) and states that the change in velocity across such a discontinuity should follow:

$$\Delta\mathbf{V} = \pm\,\Delta\mathbf{V_A}, \tag{1}$$

with

$$\mathbf{V_A} = \frac{\mathbf{B}}{\sqrt{\mu_0\rho}}\sqrt{1-\frac{\mu_0}{B^2}(P_\parallel - P_\perp)}\,, \tag{2}$$

where $\mathbf{V_A}$ is the local Alfvén velocity and $(P_\parallel - P_\perp)\,\frac{\mu_0}{B^2}$ is the pressure anisotropy correction term (with $P_\parallel$ and $P_\perp$ being the pressures parallel and perpendicular to the magnetic field, respectively). As the spacecraft crosses the exhaust, it encounters two rotational discontinuities with opposite correlations. This

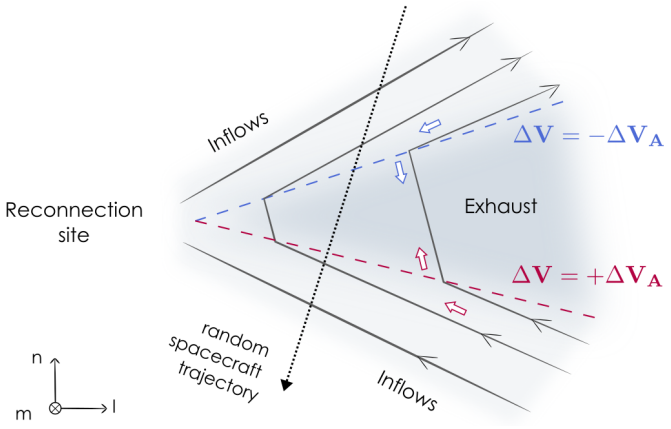

Fig. 1. Illustration of the Walén relation across a reconnection site. Magnetic field lines are drawn in black, while white arrows represent the plasma flow in the de Hoffman-Teller frame (de Hoffmann & Teller 1950). The rotational discontinuities delimiting the exhaust are shown as dashed lines, with their colour indicating which sign of the Walén relation applies at this boundary. An illustrative spacecraft trajectory is plotted as a dotted arrow. Figure adapted from Gosling et al. (2005a).

is illustrated in Fig. 1, where at each boundary, the sign of the Walén relation changes as indicated by the direction of the flow in the de Hoffman-Teller frame (de Hoffmann & Teller 1950). A spacecraft flying through the exhaust following the dotted arrow would first see an anticorrelation between $\mathbf{V}$ and $\mathbf{V_A}$ upon entry into the exhaust, followed by a correlation when exiting the exhaust.

The above signatures of magnetic reconnection were first observed in situ in the solar wind by Gosling et al. (2005a) in the interior of an interplanetary coronal mass ejection (ICME) at 1 AU. Since then, the role of magnetic reconnection has been highlighted in different contexts: it is known to occur close to or within ICMEs (Gosling et al. 2005a; Gosling & Szabo 2008), to participate in their natural erosion (Lavraud et al. 2014; Ruffenach et al. 2012, 2015), and to play a key role in the dynamics of the heliospheric current sheet (HCS) by releasing flux ropes from the tip of the helmet streamer (Gosling et al. 2005b, 2006; Lavraud et al. 2009, 2020; Sanchez-Diaz et al. 2017, 2019; Phan et al. 2021; Réville et al. 2022). Magnetic reconnection has also been observed in the regular solar wind at 1 AU (Phan et al. 2006, 2009, 2010; Davis et al. 2006; Eriksson et al. 2009; Gosling 2007; Gosling et al. 2007; Mistry et al. 2015, 2017) and is suspected to play a role in heating and accelerating the solar wind closer to the Sun (e.g., Priest et al. 2005; Klimchuk 2006), though evidence of the latter is still lacking. The Parker Solar Probe (PSP) mission has provided new insights into the role of magnetic reconnection, highlighting that in the young solar wind, magnetic reconnection is not a prevalent process, with the majority of non-reconnecting current sheets being found to be associated with transient structures called magnetic switchbacks (Phan et al. 2020). At 0.1 AU, magnetic reconnection is more frequently observed near the HCS (Phan et al. 2021) than in the regular solar wind, and the opposite is true at 1 AU.

While detecting magnetic reconnection in situ is key to furthering our understanding of energy conversion in space plasmas, the associated exhausts typically span broad scales in the time series, from seconds or below (providing the instrumental resolution is sufficiently high) to tens of minutes. As a consequence, detecting exhausts in the decades of data provided by present and past solar wind missions such as Wind, ACE, Helios, PSP, and Solar Orbiter can be an onerous task. Tilquin et al. (2020) attempted to detect reconnection jets automatically, and managed to drastically reduce the time needed to build a magnetic reconnection data set with Helios data by adopting a machine learning approach. More recently, Eriksson et al. (2022) also devised an automatic detection method and analysed ten years of WIND data based on typical reconnection signatures. Both of these studies represent significant progress towards analysing magnetic reconnection in the solar wind in a systematic way. In line with these works, here we present a new approach to automatically identify reconnection exhausts in situ using Bayesian considerations.

The objective of this work is to analyse the prevalence of magnetic reconnection in the solar wind using Solar Orbiter data. To this end, we present a new approach for automatically identifying reconnection exhausts in situ where we aim to obtain a low false-positive (FP) rate, an acceptable running time, and a reusable tool that can easily be applied by the scientific community. The method, described in Sect. 3, is inspired from the visual identification process and relies heavily on the Walén relation, as well as on Bayesian inference and physical considerations. In Sect. 4, we apply the algorithm to Solar Orbiter data from between 0.6 and 0.8 AU, where we detect 146 jets over a period of 20.7 days. We perform a statistical study on the jets we detect and discuss our results in Sect. 5. We summarize our findings in Sect. 6.

2. Data

In this paper, we use data from the Solar Orbiter spacecraft (Müller 2020), particularly the Proton and Alpha particle Sensor (PAS; Louarn et al. 2021) of the Solar Wind Analyser (SWA) suite (Owen et al. 2020) and the magnetometers of the MAG instrument (Horbury et al. 2020). We resample all data products to 0.25 Hz in order to match the time resolution of the PAS data in its normal mode. The data we use are shown in the *RTN* frame of reference, with $\mathbf{R}$ (radial) being the Sun to spacecraft unit vector, $\mathbf{T}$ (tangential) being the cross product between the Sun's spin axis and $\mathbf{R}$, and with $\mathbf{N}$ (normal) completing the direct orthogonal frame.

3. Detection algorithm

When searching for magnetic reconnection signatures in situ, we typically look for ion jets that are centred on coincidental thin, bifurcated current sheets and perform the Walén test to check whether or not the exhaust boundaries are consistent with rotational discontinuities of opposite correlations (e.g., Phan et al. 2020). It is this process, which seems quite simple at first glance, that we aim to automatise in this work.

3.1. Change of correlation

The first feature we focus on detecting is a quantifiable change of correlation. To do this, we test the Walén relation and compare different models (defined hereafter) on various scales using a sliding window method.

3.1.1. Model definitions

Let $\widehat{t}$ be a time vector centred on a time t_0 and containing N data points spaced by a constant dt. We denote $\mathbf{V}(\widehat{t})$ the velocity

vector measured by the spacecraft on this given temporal window[1] and consider the variation vector relative to the window's centre $\Delta\mathbf{V}(\widehat{t}) = \mathbf{V}(\widehat{t}) - \mathbf{V}(t_0)$. We aim to compare this relative velocity vector $\Delta\mathbf{V}(\widehat{t})$ to a modelled velocity $\Delta\mathbf{V}_{\mathcal{M}}(\widehat{t}, \boldsymbol{\theta})$, which is defined as follows:

$$\Delta\mathbf{V}_{\mathcal{M}}(\widehat{t}, \boldsymbol{\theta}) = \begin{cases} \theta_a \, \Delta\mathbf{V}_{\mathbf{A}}(\widehat{t}), & \text{if } t \leq t_0 \\ \theta_b \, \Delta\mathbf{V}_{\mathbf{A}}(\widehat{t}), & \text{otherwise,} \end{cases} \tag{3}$$

where $\Delta\mathbf{V}_{\mathbf{A}}(\widehat{t}) = \mathbf{V}_{\mathbf{A}}(\widehat{t}) - \mathbf{V}_{\mathbf{A}}(t_0)$ with $\mathbf{V}_{\mathbf{A}}$ the Alfvén speed, and where $\boldsymbol{\theta} = [\theta_a, \theta_b]^{\mathrm{T}}$ is a two-component parameter vector with $\theta_{a,b} = \pm 1$. Assuming that the regular solar wind is mostly Alfvénic (Bale et al. 2019; Louarn et al. 2021), only four cases arise, defining four models:

- $\boldsymbol{\theta}_1 = [+1, +1]^{\mathrm{T}}$ corresponds to an Alfvénic correlated solar wind,
- $\boldsymbol{\theta}_2 = [-1, -1]^{\mathrm{T}}$ corresponds to an Alfvénic anti-correlated solar wind,
- $\boldsymbol{\theta}_3 = [+1, -1]^{\mathrm{T}}$ corresponds to a correlated / anti-correlated reconnection jet,
- $\boldsymbol{\theta}_4 = [-1, +1]^{\mathrm{T}}$ corresponds to an anti-correlated / correlated reconnection jet.

In the following subsections, we compare these four models, but we underline here that the algorithm best works where the solar wind is Alfvénic as we assumed.

3.1.2. Likelihood computation

For each model, we compute the log-likelihood of the data, which quantifies the probability of observing the data assuming that this model is correct. We assume that the dispersion σ of our data $\Delta\mathbf{V}$ around its expected value $\Delta\mathbf{V}_{\mathcal{M}}$ takes on the following form:

$$\sigma(\widehat{t}) = \sigma_0 + \epsilon N \left[1 - \exp\left(\frac{1}{2} \left(\frac{\widehat{t} - t_0}{N \mathrm{d}t} \right)^2 \right) \right]. \tag{4}$$

The first term assumes a white noise model with a $\sigma_0 = 2.0\,\mathrm{km\,s^{-1}}$ dispersion. This value corresponds to the typical error on the velocity vector for the PAS instrument on Solar Orbiter, which is estimated to be between 1 and $3\,\mathrm{km\,s^{-1}}$ (Louarn et al. 2021). Increasing σ_0 decreases the number of detections, as this amounts to increasing the assumed noise on $\Delta\mathbf{V}$. The second term is introduced to account for the fact that the Alfvénicity of the solar wind may not be perfect. Therefore, the considered model is less accurate at the edges of the window as we take the reference point at its centre (especially true for large scales) and as such the dispersion should increase with distance from the centre of the window. We assume a Gaussian form with an amplitude of $\epsilon = 0.1\,\mathrm{km\,s^{-1}}$ increase in dispersion per data point.

From here, for a given $\boldsymbol{\theta}$, the likelihood of the data follows a normal distribution and may be written for each data point measured at t_i as

$$p(\Delta\mathbf{V}(t_i) \mid t_i, \boldsymbol{\theta}) = \mathcal{G}\left(\Delta\mathbf{V}(t_i),\ \Delta\mathbf{V}_{\mathcal{M}}(t_i, \boldsymbol{\theta}),\ \sigma_i^2 \mathbb{1} \right), \tag{5}$$

where $p(\Delta\mathbf{V}(t_i) \mid t_i, \boldsymbol{\theta})$ designates the probability of observing $\Delta\mathbf{V}(t_i)$ at this given time t_i knowing $\boldsymbol{\theta}$, $\mathcal{G}$ is a 3D Gaussian distribution function and $\mathbb{1}$ is the identity matrix. More explicitly, by assuming independent measurements and taking the logarithm of this expression, the log-likelihood of the data is given by (see Appendix A)

$$\ln p(\Delta\mathbf{V} \mid \widehat{t}, \boldsymbol{\theta}) = \sum_{i=1}^{N} -\frac{1}{2\sigma_i^2} |\Delta\mathbf{V}(t_i) - \Delta\mathbf{V}_{\mathcal{M}}(t_i, \boldsymbol{\theta})|^2 - \frac{3}{2} \ln(2\pi\sigma_i^2). \tag{6}$$

3.1.3. Model comparison and prior definition

The posterior probability – which quantifies the credence of a model (in our case, the value of $\boldsymbol{\theta}$) given the observed data (i.e. the values of $\Delta\mathbf{V}$ on the time window $\widehat{t}$) – is then computed through the Bayes equation:

$$\ln p(\boldsymbol{\theta} \mid \widehat{t}, \Delta\mathbf{V}) = \ln p(\boldsymbol{\theta} \mid \widehat{t}) + \ln p(\Delta\mathbf{V} \mid \widehat{t}, \boldsymbol{\theta}) - \ln p(\Delta\mathbf{V} \mid \widehat{t}), \tag{7}$$

where $\ln p(\Delta\mathbf{V} \mid \widehat{t})$ is a constant of $\boldsymbol{\theta}$, and $p(\boldsymbol{\theta} \mid \widehat{t})$ is the prior probability on the $\boldsymbol{\theta}$ parameter for our given window, which represents the a priori probability of observing an exhaust in the solar wind. Given each posterior probability, $p(\boldsymbol{\theta} \mid \widehat{t}, \Delta\mathbf{V})$, we may compare the probability of observing a jet to the probability of observing an Alfvénic solar wind using Bayesian inference and defining the posterior ratio:

$$\frac{p(\text{jet}|\, \widehat{t}, \Delta\mathbf{V})}{p(\text{no jet}|\, \widehat{t}, \Delta\mathbf{V})} = \frac{p(\boldsymbol{\theta}_3|\, \widehat{t}, \Delta\mathbf{V}) + p(\boldsymbol{\theta}_4|\, \widehat{t}, \Delta\mathbf{V})}{p(\boldsymbol{\theta}_1|\, \widehat{t}, \Delta\mathbf{V}) + p(\boldsymbol{\theta}_2|\, \widehat{t}, \Delta\mathbf{V})}, \tag{8}$$

where $p(\text{jet}|\, \widehat{t}, \Delta\mathbf{V})$ designates the probability that the points in the time window $\widehat{t}$ are part of a reconnection jet given the data $\Delta\mathbf{V}$. As described above, this event can occur in one of two ways: a correlated–anticorrelated or an anticorrelated–correlated reconnection exhaust (i.e. θ_3 or θ_4). On the other hand, the probability $p(\text{no jet}|\, \widehat{t}, \Delta\mathbf{V})$ is composed of the two events θ_1 and θ_2, corresponding to the case of an Alfvénic wind. All the terms of Eq. (8) can be computed with the help of Eq. (7). As such, the evaluation of this ratio remains numerically challenging, and we show in Appendix A that a relevant equivalent can be defined as

$$\begin{aligned} Q(\widehat{t}) &= \left(\frac{p\left(\text{jet}|\, \widehat{t}, \Delta\mathbf{V}\right)}{p\left(\text{no jet}|\, \widehat{t}, \Delta\mathbf{V}\right)} \right)^{1/N} \\ &\simeq p(\text{jet}|\, \widehat{t})^{\frac{1}{N}} \frac{\sum_{k=3,4} p(\Delta\mathbf{V}|\, \widehat{t}, \boldsymbol{\theta}_k)^{\frac{1}{N}}}{\sum_{k=1,2} p(\Delta\mathbf{V}|\, \widehat{t}, \boldsymbol{\theta}_k)^{\frac{1}{N}}}, \end{aligned} \tag{9}$$

where $p(\text{jet}|\, \widehat{t})$ designates the prior probability, which is defined as the probability that all points in the time window $\widehat{t}$ are part of a reconnection jet. The main benefit of using Eq. (9) instead of Eq. (8) lies in the presence of much larger terms in the sums, allowing their evaluation without truncation errors. The only remaining factor that needs to be defined in order to compute $Q(\widehat{t})$ is the prior probability $p(\text{jet}|\, \widehat{t})$.

Defining the prior probability is an important step in the detection algorithm, as it amounts to setting a threshold on the detection. Let us assume that each data point has a 1% chance of being part of a reconnection exhaust. This value is taken based on the study of Lavraud et al. (2021), as the six exhausts they detect in one day represent around 1% of the data. Let us underline here that the 1% value is not conservative, and in Appendix B we show that decreasing this value leads to a better performance of the algorithm; it might be adjusted in future work. This value being fixed, the prior probability for a

[1] In this section, all vectors depending on $\widehat{t}$ ($\mathbf{V}(\widehat{t})$, $\Delta\mathbf{V}(\widehat{t})$, $\Delta\mathbf{V}_{\mathcal{M}}(\widehat{t}, \boldsymbol{\theta})$, etc.) have a dimension of $3 \times N$.

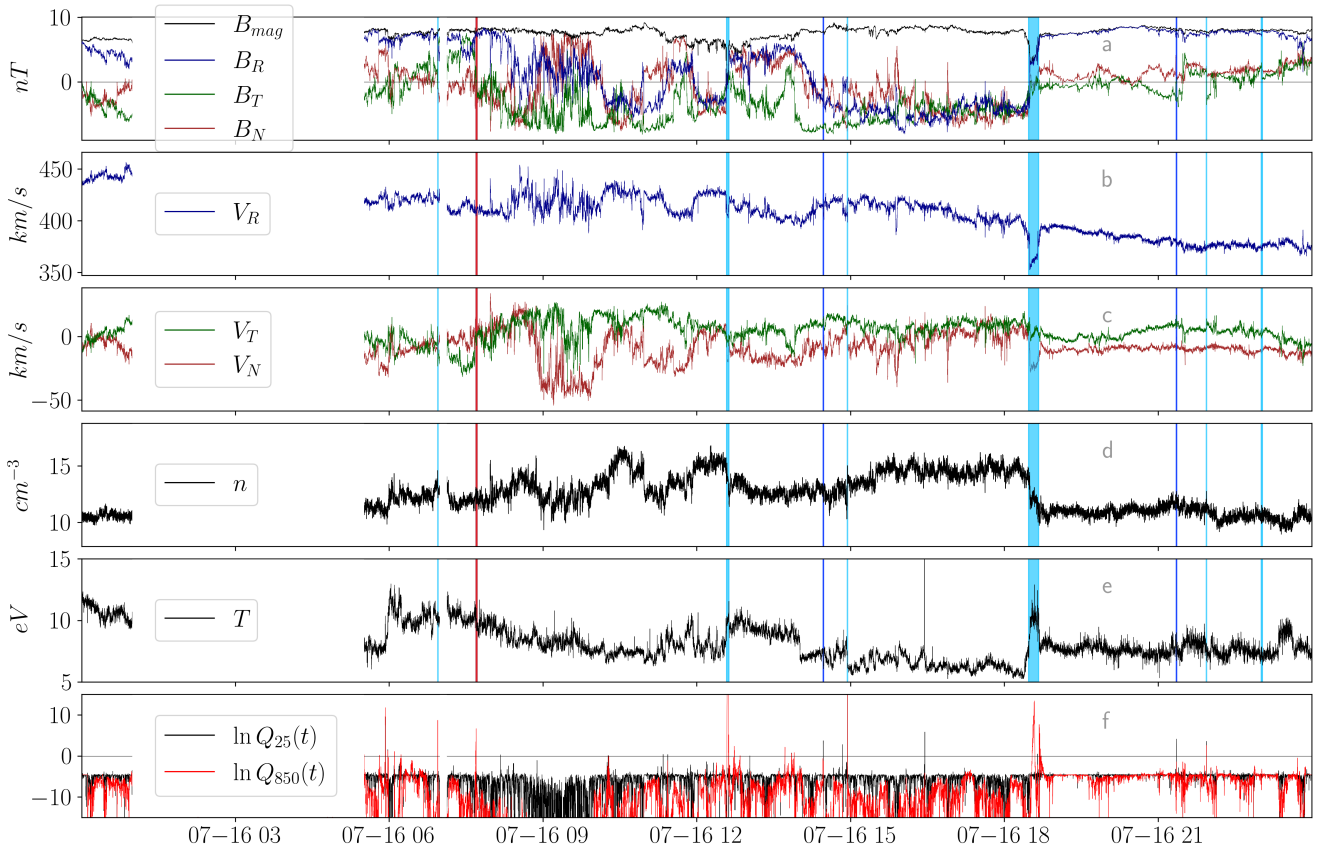

Fig. 2. Automated detection of reconnection exhausts on July 16, 2020. We show the magnetic field components and its amplitude in panel a, the ion velocity vector components in panels b and c, the ion density in panel d, and the ion temperature in panel e. Panel f displays the quantity $\ln Q_{25}(t)$ and $\ln Q_{850}(t)$ (see Sect. 3.1). The shaded areas indicate the final detections made by the algorithm (see Sect. 3.2). We show the six reconnection jets that were also detected by Lavraud et al. (2021) in light blue, two new true detections in darker blue, and one false detection in red.

given window is then given by $p(jet \mid \widehat{t}) = 0.01^N$. The fact that this probability decreases with N exponentially is the result of assuming that each point of $\widehat{t}$ has an independent probability of being part of a jet. Naturally, it is likely in practice for successive points to be correlated, and it is therefore likely that the probability of the time window being part of a jet is the result of an underlying stochastic process that is a function of time. The careful estimate of the nature of this process is an issue that would probably necessitate an entire study. As it is, this exponential decrease with N must therefore be seen as a lower bound of the prior $p(\text{jet}|\widehat{t})$, in addition to being easy to implement and compute. Taking this term to the power $1/N$ in Eq. (9) allows us to get rid of most of the window's size dependence on the posterior ratio by using $Q(\widehat{t})$. We can then evaluate Eq. (9) for any time window, and a change of correlation is detected on our considered window if the posterior ratio is superior to 1, or equivalently if the scalar value $\ln Q(\widehat{t})$ is positive.

3.1.4. Expanding to the complete data set

Until now, we have only considered a given time window $\widehat{t}$, characterised by its centre t_0 and width N. For this time window, we computed a scalar value, which is the probability of observing a correlation change given the observed data in this window. This quantity can be written $Q(t_0, N)$ or equivalently $Q_s(t_0)$, with the subscript s designating the scale of the temporal window $N\mathrm{d}t$. Let us now expand to a complete data set characterised by a time vector t. To sweep through this data set, we only need to repeat the process described immediately above while shifting t_0. This yields a continuous log-probability over time $Q_s(t)$. To detect correlation changes on different scales, we start from small scales and gradually increase the window size s. A potential jet is flagged whenever the quantity $\ln Q_s(t)$ becomes positive for at least two consecutive points, and we only flag an interval if it has not been detected at lower scales. This process (going from small to large scales) allows us to detect an exhaust on the minimum scale possible, which permits us to accurately account for its duration.

3.1.5. Application to data from July 16, 2020

As an illustration we apply this first part of the detection algorithm to 24h of data obtained on July 16, 2020, and presented in Fig. 2. This day was studied in detail by Lavraud et al. (2021), who identified six reconnection exhausts, which are highlighted as light blue shaded areas in Fig. 2. We show the magnetic field and ion data in the first five panels for this day for context. We ran the detection algorithm, investigating 100 scales starting from 25 s up to 850 s, and we display $\ln Q_{25}(t)$ and $\ln Q_{850}(t)$ in Fig. 2f. The six reconnection exhausts identified by Lavraud et al. (2021) and highlighted in light blue all correspond to positive values of $\ln Q(t)$ for one or the other scale, except for the last jet observed at 23:01 UT. The latter is actually detected by the algorithm at intermediate scales.

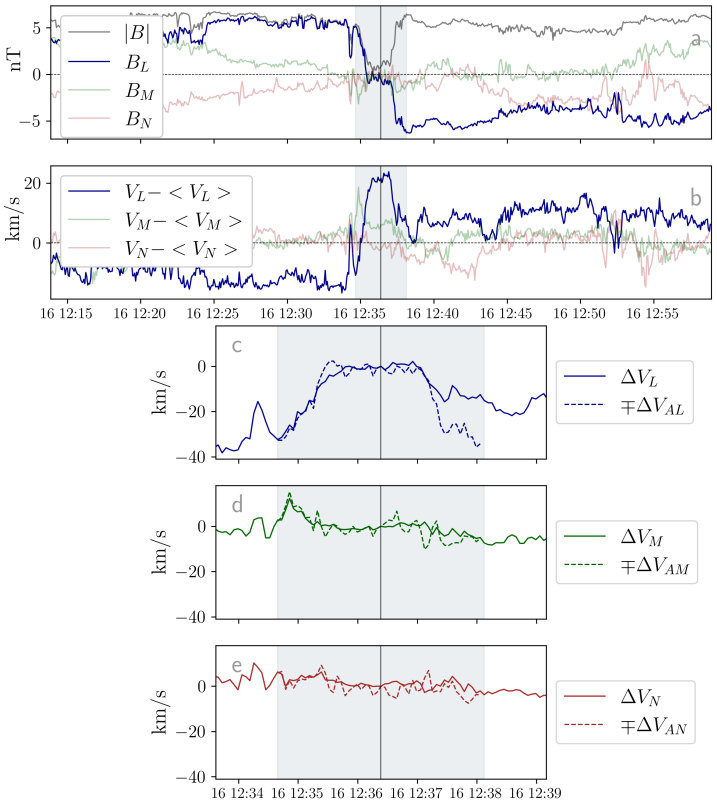

Fig. 3. Illustration of the Walén relation for the reconnection jet occurring on July 16, 2020, between 12:34:39 and 12:38:07 (Lavraud et al. 2021). Panel *a* displays the magnetic field and panel *b* the variation of the ion velocity vector around its mean value. Both are transformed in the *lmn* frame using a minimum variance analysis (Sonnerup & Cahill 1967). The grey area highlights the jet location. Panels *c* to *e* show zooms onto the jet and compare the quantities $\Delta\mathbf{V}$ (full lines) and $\mp\Delta\mathbf{V_A}$ (dashed lines), with the change of correlation occurring at the centre of the jet (black vertical line).

In Fig. 3, we illustrate the Walén relation for one of the reconnection jets identified by Lavraud et al. (2021) on July 16, 2020, around 12:36, which our algorithm picks up as well. In Figs. 3*c* to 3*e*, it is clear that $\Delta\mathbf{V}$ and $\mp\Delta\mathbf{V_A}$ correspond to one another. Any other value of θ ($+\Delta\mathbf{V_A}$,$-\Delta\mathbf{V_A}$, $\pm\Delta\mathbf{V_A}$) would not show a better fit to $\Delta\mathbf{V}$. Interestingly, the reconnection jet seems to be Alfvénic on its leading edge (jump in ion speed around 40 km s^{-1}) and sub-Alfvénic on the trailing edge (20 km s^{-1}).

After this first part of the algorithm, all intervals where $\ln Q(t)$ is positive (Fig. 2f) are flagged, and while some of them are true new detections, others are false positives. The second part of the algorithm is designed to differentiate between true and false detections based on some physical considerations.

3.2. Jet confirmation

3.2.1. B_l reversal

The first step we take is to transform each interval to its associated *lmn* frame using the minimum variance analysis technique (Sonnerup & Cahill 1967). Similarly to Tilquin et al. (2020), we impose that the B_l component should reverse over the interval. We additionally require that the sign of B_l remains the same over 10% of the window length at the beginning and end of the window.

3.2.2. The existence of a jet

We ensure that a velocity jet is indeed observed along the l direction. We require that:

- The signs of the V_l variation between the centre of the window and both edges of the interval are the same, meaning that $\mathrm{sign}(V_l(t_0) - V_l(t_i)) = \mathrm{sign}(V_l(t_0) - V_l(t_f))$, with t_i and t_f being the start and end time of the window;
- The maximum V_l variation is superior to the maximum variations of V_m and V_n;
- The V_l variation between the centre of the window and both edges of the interval should be at least 30% of the maximum V_l variation.

The first requirement is enforced in order to discard changes of correlations that are associated with a **V** rotation (instead of a **B** rotation); the second point ensures that the jet is observed in the l component; and the third point discards intervals where V_l does not display a sufficiently clear jet signature. This latter point is introduced at the expense of removing the most asymmetric reconnection cases.

3.2.3. A condition on the electric current

During a change of correlation coincidental with a current sheet, there always exists a magnetic shear and an associated current. In the limit of null magnetic shear and current, magnetic reconnection may not occur, but this constitutes a singularity. In practice, we should define a minimum current for our algorithm to detect an exhaust. Current measurements are not available as a data product on Solar Orbiter, and therefore we devise a 1D approximation for the electric current based on the Maxwell Ampere equation. In the *lmn* frame, the rotational of **B** writes:

$$\nabla \wedge \mathbf{B} = \begin{bmatrix} \partial_m B_n - \partial_n B_m \\ \partial_n B_l - \partial_l B_n \\ \partial_l B_m - \partial_m B_l \end{bmatrix}. \tag{10}$$

We assume no variation of **B** along m ($\partial_m = 0$), and we neglect the terms $\partial_n B_m$, $\partial_l B_m$, and $\partial_l B_n$ compared to the B_l variation. Indeed, **l** is the direction of maximum variance of the magnetic field, and the Hall field (B_m) should be negligible far from the reconnection site while B_n should remain essentially constant throughout the exhaust. To first order, the equation can therefore be simplified to

$$\nabla \wedge \mathbf{B} = \partial_n B_l \mathbf{u_m}, \tag{11}$$

where $\mathbf{u_m}$ is the unit vector in the m direction. From there, we may derive an approximation for the electric current:

$$j_e = \frac{\Delta B_l}{\mu_0 \Delta n}. \tag{12}$$

The term ΔB_l is computed at the edges of our considered window, and $\Delta n = V_n \Delta t$. Following some tests of trial and error, we set the minimum current required for detection at $j = 0.04$ nA/m^2.

3.2.4. Application to data from July 16, 2020

We now apply the complete algorithm to July 16, 2020, and scan 100 scales between 25 s and 850 s. We detect nine potential reconnection events over this day, which are displayed in Fig. 2. The algorithm accurately finds the six reconnection jets (light blue intervals) identified in Lavraud et al. (2021) and

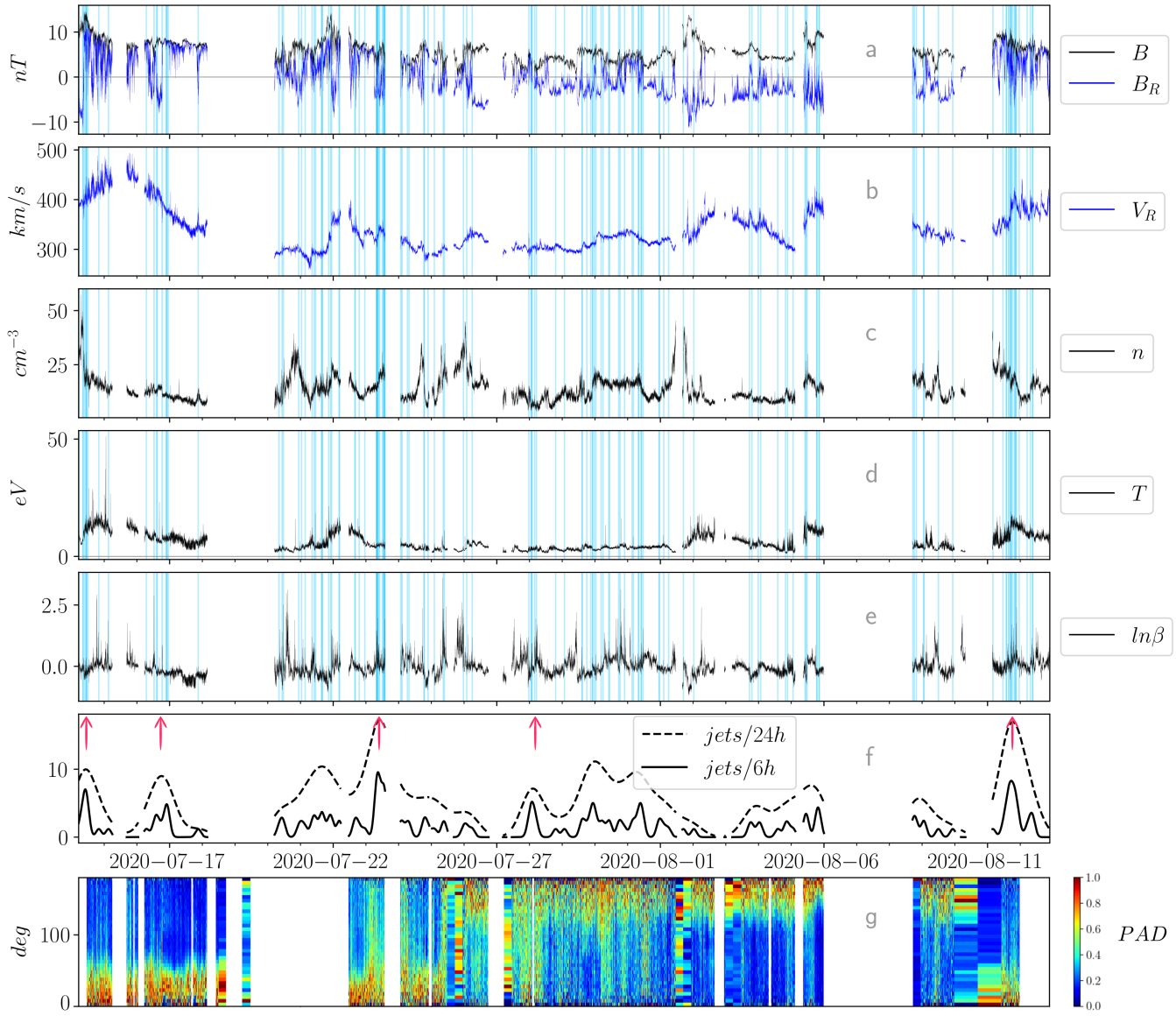

Fig. 4. Reconnection exhaust detections over 30 days of data from July 14, 2020, at 05:15 to August 13, 2020, at 00:00. Panels *a* and *b* show the magnetic field components and its amplitude, panels *c* and *d* display the ion velocity vector components, and panel *e* shows the ion density. The blue shaded areas indicate the location of the reconnection exhausts we confirmed (see Table D.1) and panel *f* displays their occurrence computed on both a 6h and a 24h window. The red arrows highlight intervals of higher occurrence. Panel *g* shows the PAD of suprathermal electrons (with energy superior to 120 eV) normalised to its maximum value in each time bin.

adds two new true detections (dark blue intervals). One interval (07:41:47–07:42:55) is flagged by our algorithm but is not a reconnection exhaust (red interval). False detections are further discussed in Sect. 4.1.

3.3. Assumption summary

In the algorithm presented above, several assumptions and requirements impact the detection and some may be improved in the future. We list them here for the sake of clarity:

- We assume a dispersion σ in the form of Eq. (4) with a typical dispersion of $\sigma_0 = 2\,\mathrm{km\,s^{-1}}$ (Louarn et al. 2021) and an increasing uncertainty of $\epsilon = 0.1\,\mathrm{km\,s^{-1}}$ per point. Increasing σ_0 decreases the number of detections, and this value should be adapted to the mission considered.
- We assume a prior probability $p(jet|t_i)$ of 1% based on Lavraud et al. (2021). Decreasing $p(jet|t_i)$ decreases the number of detections, and this value might need to be adapted for different regions of the heliosphere.
- A correlation change is detected on a minimum of two consecutive points.
- B_l should reverse over the interval (Tilquin et al. 2020).
- The sign of B_l should remain stable over 10% of the window length at the beginning and end of the window.
- The maximum V_l variation should be superior to the maximum variations of V_m and V_n.
- The V_l variation should be at least 30% of the maximum V_l variation at each exhaust boundary.
- The electric current on the interval should be greater than $0.04\,\mathrm{nA/m^2}$.

While some of these values are justified by physical considerations and previous work, others have been set based on the results of trial and error. Future investigation on how to set these parameters might further improve the detection algorithm.

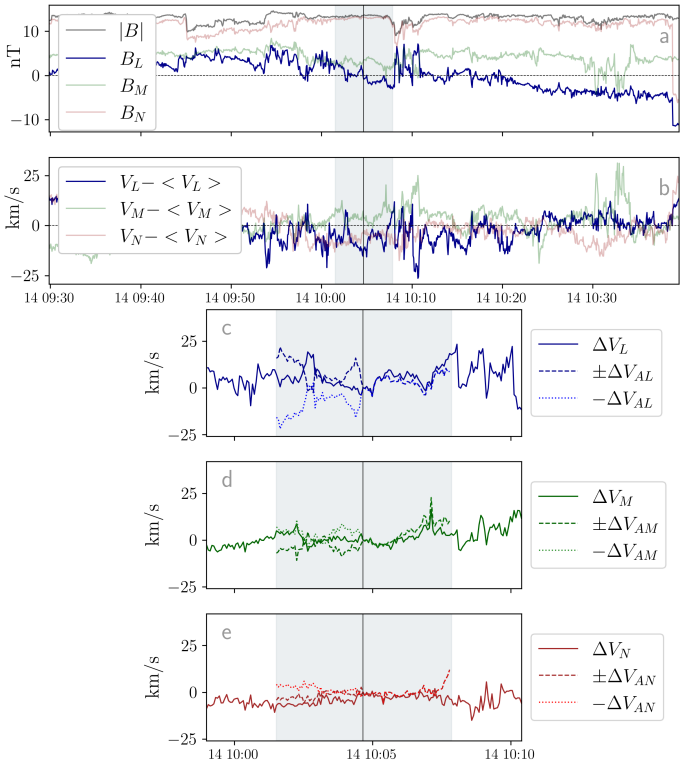

Fig. 5. Illustration of a false detection occurring on July 14, 2020, between 10:01:31 and 10:07:51. Panels *a* and *b* are similar to those of Fig. 3. Panels *c* to *e* compare the quantities $\Delta\mathbf{V}$ (full lines), $\pm\Delta\mathbf{V_A}$ (dashed lines), and $-\Delta\mathbf{V_A}$ (dotted lines).

A performance analysis of the algorithm is available in Appendix B, and shows the impact of changing some of the input parameters. The detection algorithm is publicly available[2].

4. Statistical results

4.1. Algorithm performance

We apply the detection algorithm described in Sect. 3 to Solar Orbiter data running from July 14, 2020, at 05:15 to August 13, 2020, at 00:00. During this period of about a month, Solar Orbiter measured the solar wind properties from 0.63 AU to 0.82 AU and we display the solar wind properties in Fig. 4. The data gaps (Table C.1) in Fig. 4 are due to the absence of either magnetic field or plasma measurements and amount to 9 days of missing data; we therefore investigate a total of 20.7 days of Solar Orbiter measurements. During this period, the algorithm detects 270 potential jets, and through visual inspection of these detections we are able to confirm 133 (49%) reconnection events and reject 137 (51%) false detections.

Such false detections are typically due to deviations from a unique Alfvénicity sign produced at small scales compared to the window length, and we show an example in Fig. 5. There, even though the algorithm detects a change of correlation, a B_l reversal, sufficient current, and sufficient V_l variation, this event cannot be identified as a reconnection jet. By contrast with Fig. 3, no obvious current sheet or ion jet is observed in panels a and b. In panels c to e, we see that $\pm\Delta\mathbf{V_A}$ shows better agreement with $\Delta\mathbf{V}$ than $-\Delta\mathbf{V_A}$ does, even though the anticorrelation is clear on the leading edge of the interval. This is due to a slight deviation from Alfvénicity close to the centre of the window, which leads to large errors between $\Delta\mathbf{V}$ and $-\Delta\mathbf{V_A}$. Another cause for false detection (not shown) is that, despite displaying a change of correlation and other required signatures (Sect. 3.2), the presence of a jet is not sufficiently clear, for instance lacking evidence in terms of density, temperature, magnetic field magnitude, and so on. This is the case for the false detection of July 16 (07:41:47-07:42:55) presented in Sect. 3.1.5.

One of the aims of this study is to analyse reconnection jets in the solar wind in a close-to exhaustive way. Therefore, we chose thresholds on the input parameters that were not conservative so as to increase the number of detections and include even the shortest jets. This leads to a high FP rate (51%); however, it remains a goal of the authors to decrease this rate in the future while detecting as many jets as possible. Adjusting some input parameters of the current version of the algorithm already allows a decrease in the FP rate, but at the expense of a decrease in the number of detections. For instance, increasing the assumed noise on the PAS data from 2 km s^{-1} to 5 km s^{-1} leads to 57 detections, among which 50 (88%) are reconnection jets and 7 (12%) are false detections. A performance analysis of the algorithm is available in Appendix B.

The overall process of running the algorithm and checking the different detections amounts to 4 to 5 h of work, which is a significant decrease compared to the time required for finding jets with visual inspection alone. In parallel, we were able to visually identify 13 additional reconnection exhausts that were missed by the detection algorithm. These 13 detections are not exhaustive and additional work is required to estimate the false-negative rate of the algorithm. We display the times of the 146 (133+13) reconnection jets we detected in Fig. 4. We also provide the detailed start and end times in Table C.1. These start and end dates have been redefined visually to best fit the identified reconnection jets, and the error made by the algorithm on the boundaries is around 16% of the jet duration on average.

4.2. Occurrence rate and waiting time

The occurrence rate computed over a 24h window is plotted in Fig. 4f and we find a global average of 7.0 jets/day. It is visually striking in Fig. 4 that there exist periods of time in the solar wind where a large number of reconnection jets occur (red arrows), while other periods are completely devoid of events. This clustering is made particularly clear by the occurrence rate computed over 6 hours, which sometimes peaks at 10 events/6h (e.g., July 23) or stays close to zero for extended periods (e.g., July 17, August 2–3). We further confirm the clustering of reconnection jets in the solar wind by analysing the waiting time[3] distribution of our reconnection exhausts. If the occurrence was random, as per a Poisson process, we would expect the waiting time distribution to follow an exponential law with distribution re^{-rt}, with r the occurrence rate and t the waiting time. In Fig. 6, we display the observed distribution of the jet waiting time together with the expected Poisson distribution. While the exponential curve reproduces the overall trend of waiting times, it does not account for the amount of observed waiting times below 20 min (two first bars of the histogram). Long waiting times (>1200 min) are also unlikely for a Poisson process. We further confirmed this result by performing this analysis on a previous version of the magnetic field dataset (L2 V2, not shown), which contains fewer data gaps. By including 24.3 days of data instead of 20.7, the clustering of jets becomes even clearer, with waiting times

[2] https://github.com/Nfargette/Magnetic_reconnection/

[3] Time elapsed in between two consecutive jets.

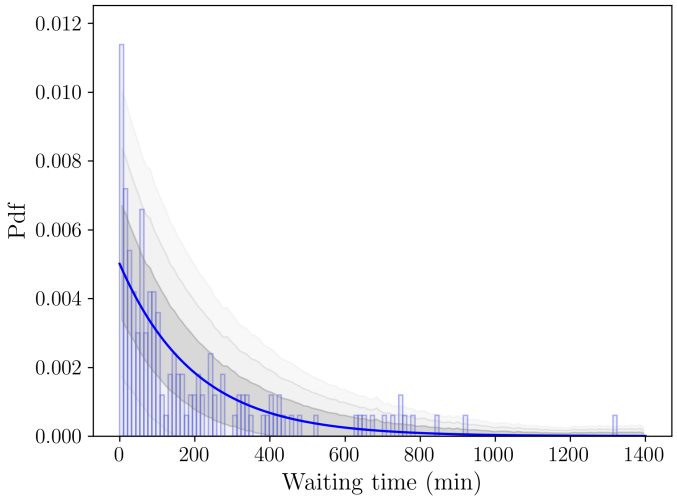

Fig. 6. Waiting time distribution of reconnection jets. The blue curve indicates the expected distribution for a random Poisson process and its associated uncertainty (1–3σ, grey shaded areas). A preliminary version of this figure is available in Woodfield et al. (2023), which is based on a previous version of Solar Orbiter data.

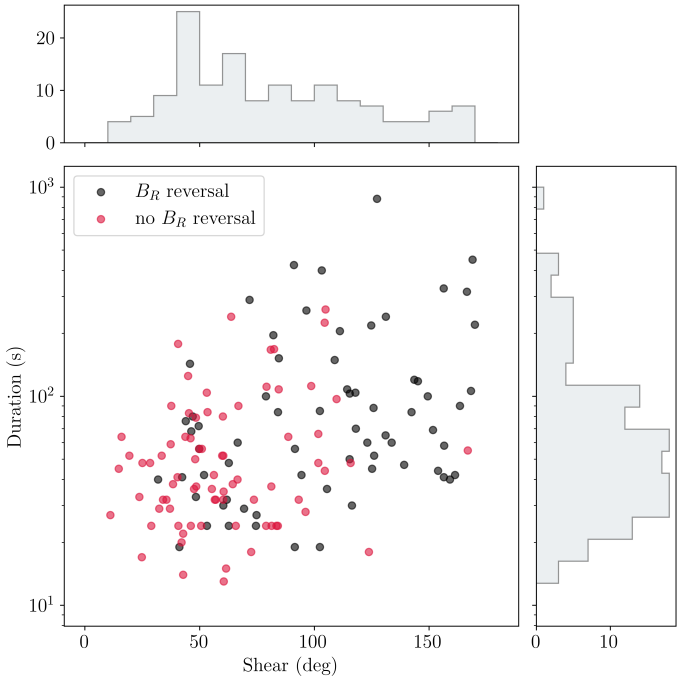

Fig. 7. Jet duration and shear across the exhaust. Red events show no reversal of the B_R component across the exhaust.

below 40 min being anomalous (more than two standard deviations away) compared to the Poisson distribution.

The fact that reconnection jets seem to cluster in the solar wind has in fact been pointed out on a larger scale. While studying 34 reconnection exhausts specifically occurring in high speed streams over 1 year of Wind data, Gosling (2007) found that while some exhausts clustered and where separated by around 2 h, numerous long intervals of several days at a time displayed no reconnection signatures. With our extended dataset, we find that this clustering is also present over one month of data regardless of the solar wind speed.

4.3. Jet properties

In Fig. 7, we show a scatter plot of the duration of reconnection jets as a function of the magnetic shear across the exhaust. The latter was computed by taking the **B** values at the jet boundaries. We see that most of our jets occur at low shear angle (<90°), which is consistent with previous studies of reconnection jets in the solar wind and reflects the fact that low shear current sheets are frequent in the solar wind (Gosling et al. 2007; Phan et al. 2010; Mistry et al. 2017; Tilquin et al. 2020; Eriksson et al. 2022). The duration of the exhaust mostly stays below 100 s, and longer jets tend to present a higher magnetic shear angle. The fact that we do not detect long low shear jets might be a detection bias as the thresholds we put on the jump in velocity and the electric current would probably reject those detections. When we convert the jet duration to width using the normal crossing velocity V_n and assuming that the ion skin depth is d_i = 100 km at 0.7 AU (Verscharen et al. 2019), we find exhaust width ranging from 6 to 1116d_i, with a median of 85d_i.

We further highlight in red the reconnection jets where the B_R component of the magnetic field is not reversed, indicating that they are not associated with a crossing of the HCS and probably occur in the turbulent solar wind. These types of jets constitute the majority of the low-shear/low-duration exhausts that we detect. For the remaining jets, which reverse the B_R component, further analysis is required to precisely determine the context in which they occur.

4.4. Solar wind conditions

In order to identify a trigger of magnetic reconnection, we investigate different solar wind parameters upon its occurrence. In Fig. 8, we display the joint distribution of the solar wind speed V, density n, temperature T, and plasma parameter $\log\beta$ for the whole period of measurements in a corner plot. In the 1D distributions (top panels), we superimpose the distribution of the exhaust inflow conditions, which were computed as the median value of the different parameters on each side of the jets in a window lasting 30% of the jet duration.

We observe several interesting differences between the standard solar wind parameter distributions (black histograms) and the solar wind conditions where magnetic reconnection occurs (blue histograms). We first observe a small tendency for the jets to be less likely to occur in the very slow solar wind (around 300 km s^{-1}). This also holds for lower wind temperatures (<3 eV) due to the correlation between solar wind speed and temperature (e.g., Burlaga & Ogilvie 1970, Lopez & Freeman 1986). Magnetic reconnections occur less frequently in conditions of higher solar wind speed (>435 km s^{-1}), but such conditions represent a minority in the dataset. In addition, there exists a clear decrease in the occurrence of reconnections at low density (<10 cm^{-3}). For the density, the mode of the standard distribution is not reproduced by the inflow condition distribution.

5. Discussion

Using the novel methodology we present in Sect. 3, we obtain an occurrence rate of 7.0 reconnection jets per day over 20.7 days of data, which is higher than previously reported. By way of comparison, occurrence rates of 1.5 day^{-1} (Gosling et al. 2007), 0.4 day^{-1} (Phan et al. 2010), and 0.88 day^{-1} (Eriksson et al. 2022) were found using the Wind spacecraft data at 1 AU, which are of a similar time resolution (3 s) to data from Solar Orbiter (4 s). The lower reconnection rates found by Gosling et al. (2007) and

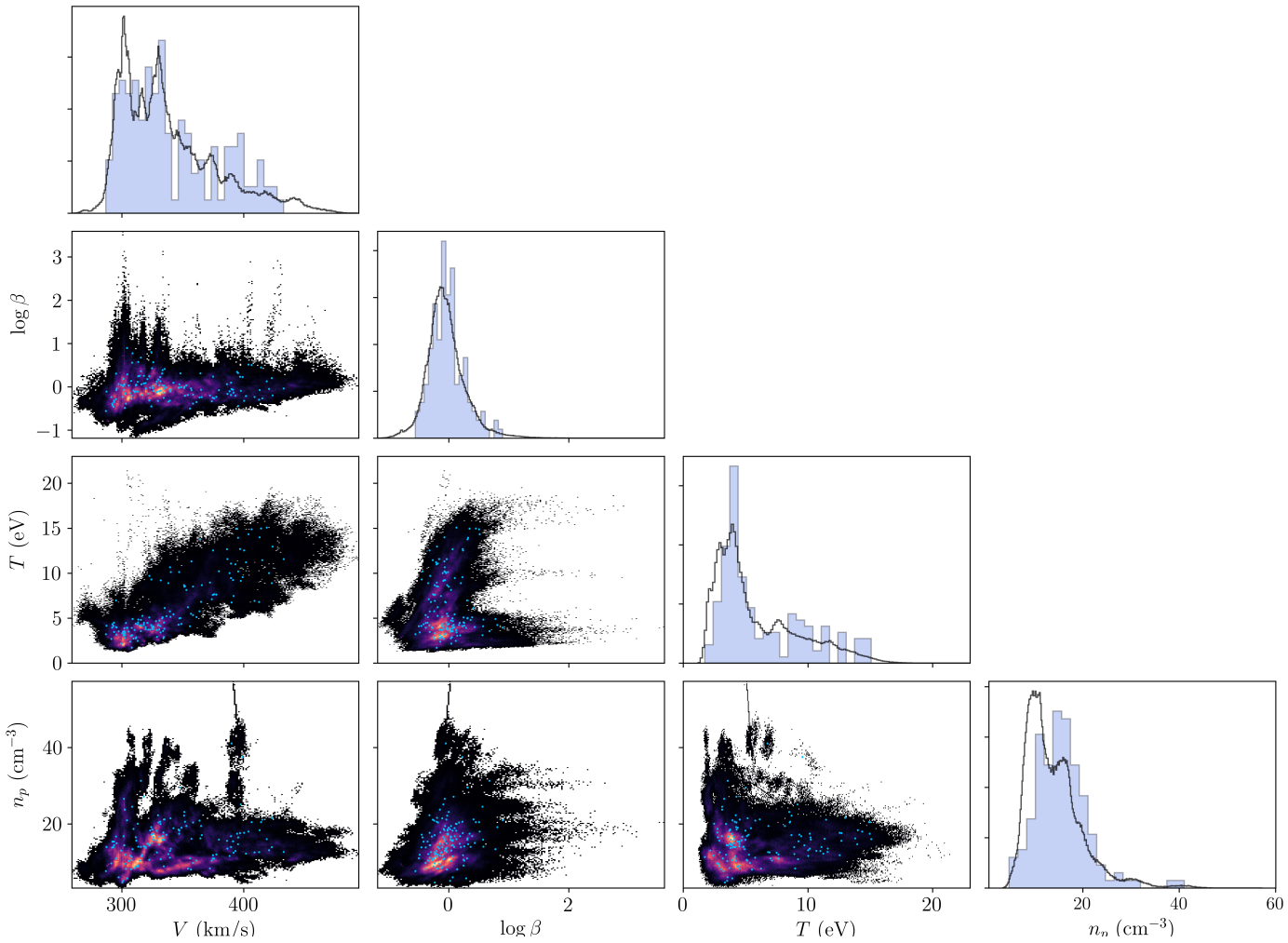

Fig. 8. Solar wind conditions upon the occurrence of magnetic reconnection. The corner plot shows the joint 2D distributions of the solar wind speed V, plasma parameter $\log\beta$, temperature T, and density n for the whole period of measurements. The superimposed blue dots indicate the value of these parameters around the intervals where magnetic reconnection was observed. The top panels of the corner plot then show the 1D histograms of these quantities for the whole month (in black) and for reconnection inflow conditions (in blue).

Phan et al. (2010) are probably due to the visual method of detection used rather than the effect of radial distance. In future work, we shall investigate the occurrence of magnetic reconnection at varying distances from the Sun. The 0.88 day^{-1} rate found by Eriksson et al. (2022), also using an automated method, is significantly lower than the 7 day^{-1} rate we observe. One potential explanation is that Eriksson et al. (2022) investigate six discrete timescales (between 12 s and 20 min) whereas we span 100 (between 25 s and 14 min). Eriksson et al. (2022) acknowledge this and state in their work that the set they observe 'should be considered as the tip of the proverbial iceberg'. An application of our algorithm to WIND data for comparison is left for future work. In total, the reconnection exhausts we detect take up 0.7% (3.5 h) of our 20.7 days of data, and the average jump in velocity in the l direction is 6^{+13}_{-4} km s^{-1}. Similarly to the conclusion of Gosling et al. (2007), these rather low values lead us to believe that these reconnection exhausts do not play a dominant role in heating and accelerating the solar wind near 0.7 AU.

In Sect. 4.2, we show that, rather than occurring randomly, reconnection exhausts tend to cluster in the solar wind. The reason for this clustering remains unclear, but several explanations can be put forward. It is possible that proximity to the HCS leads to the observation of more events. This is typically observed closer to the Sun in the PSP data (Phan et al. 2020, 2021; Lavraud et al. 2020) where the HCS is constantly reconnecting. By looking at the radial component of the magnetic field and at the 100 s resolution pitch angle distributions (PAD) of high-energy electrons (>120 eV) in Fig. 4, we can state that the HCS is probably around July 25 and again around August 11. Additional HCS crossings or partial crossings might also occur in the data set. However, the occurrence of reconnection events does not seem to particularly increase close to these dates compared to the rest of the month. We find that from the 42 events that occur less than 40 min after another event, 24 (57%) reverse their B_R component while the other 18 do not. This proportion is slightly higher compared to the proportion of the total number of events that reverse their B_R (46%). It is therefore possible that skimming of the HCS accounts for part of the clustering. However, we may not be sure that a B_R reversal is associated with a crossing of the HCS, and the distance to the HCS may not explain the periods we observe that show a drop in occurrence. We therefore explored other potential explanations for the clustering of reconnection jets.

In order to identify a potential trigger for magnetic reconnection, we investigated the prevailing solar wind conditions in the inflow regions (Sect. 4.4). We show that reconnection is

Table 1. Interval of solar wind streams resembling the fast solar wind and with low magnetic reconnection occurrence.

Start	End
2020-07-14 15h	2020-07-16 05h
2020-07-17 17h	2020-07-18 12h
2020-08-02 00h	2020-08-05 00h

less likely to occur in the tenuous (<10 cm^{-3} near 0.7 AU) solar wind. These periods correspond to streams mostly devoid of reconnection exhausts occurring on July 14-15, July 17-18, July 26-27, and August 2-3. A potential explanation might lie in the nature and origin of these particular streams. The solar wind is classically divided into two types of wind, which differ in velocity range, density, composition, variability, and origin. The fast solar wind can be traced back to coronal holes and open magnetic field lines in the low corona (e.g., Cranmer 2009), while the origin of the slow solar wind is less clear and appears to be associated with the boundaries of coronal holes (e.g., Wang 1994) or with the release of transients through magnetic reconnection at the tip of the coronal streamer (e.g., Lapenta & Knoll 2005; Antiochos et al. 2011; Sanchez-Diaz et al. 2017). Several studies have shown that there exists a type of slow solar wind that shows the characteristics of the fast solar wind in terms of Alfvénicity, composition, and density (e.g., Marsch et al. 1981; D'Amicis & Bruno 2015; D'Amicis et al. 2019). A recent study focussing on the solar wind stream occurring from July 14 to July 18, 2020, showed that it actually corresponds to a slow Afvénic solar wind stream, showing the characteristics of a fast wind stream and originating from a coronal hole (D'Amicis et al. 2021). In our one-month interval, three streams (Table 1) display a low occurrence rate of magnetic reconnection while displaying a high degree of Alfvénicity. Let us point out here that these periods of increased Alfvénicity are also the periods where the algorithm should perform best (see Sect. 3.1), and yet where the algorithm detection rate is the lowest. These streams actually resemble the switchback structures observed by the PSP mission (Bale et al. 2019; Kasper et al. 2019) with a near constant B magnitude and frequent B_R reversals. We know that magnetic reconnection is less frequent both in the turbulent high-speed solar wind (Gosling 2007) and in the highly Alfvénic slow solar wind observed by PSP close to the Sun (Phan et al. 2020). It is therefore possible that the source of the solar wind together with its degree of Alfvénicity play a role in the onset of magnetic reconnection in the solar wind.

6. Conclusions

The key findings presented in this paper can be summarised as follows.

- We present a new methodology to detect magnetic reconnection exhausts in the solar wind (Sect. 3). This automatic algorithm relies on the Walén relation, Bayesian inference, and additional physical considerations. The detection algorithm is publicly available[4].
- We apply it to one month of Solar Orbiter data while the spacecraft was located near 0.7 AU. We are able to confirm the observation of 146 reconnection exhausts over this period of observation, leading to an occurrence rate of 7 day^{-1}, which is higher that previously reported (Sect. 5).
- The reconnection exhausts we detect are mostly low shear and of short duration, consistent with the observations made at 1 AU (Phan et al. 2010).
- We find that reconnection jets tend to cluster in the solar wind, as their occurrence is not reproduced by a random distribution. We show that they are less likely to occur in the tenuous solar wind.
- We discuss potential reasons for the inhomogeneity of magnetic reconnection occurrence and propose a link to the source and Alfvénicity of the solar wind (Sect. 5).

By providing a tool to quickly identify potential magnetic reconnection exhausts in situ, we pave the way for broader statistical studies on magnetic reconnection in diverse plasma environments.

[4] https://github.com/Nfargette/Magnetic_reconnection/

Acknowledgements. Solar Orbiter is a space mission of international collaboration between ESA and NASA, operated by ESA. Solar Orbiter Solar Wind Analyser (SWA) data are derived from scientific sensors which have been designed and created, and are operated under funding provided in numerous contracts from the UK Space Agency (UKSA), the UK Science and Technology Facilities Council (STFC), the Agenzia Spaziale Italiana (ASI), the Centre National d'Études Spatiales (CNES, France), the Centre National de la Recherche Scientifique (CNRS, France), the Czech contribution to the ESA PRODEX programme and NASA. SWA work at UCL/MSSL was supported under STFC grants ST/W001004/1 and ST/X/002152/1. Solar Orbiter magnetometer data was provided by Imperial College London and supported by the UK Space Agency. Work at IRAP was supported by CNRS, CNES and UPS. The work of N. Fargette and J.P. Eastwood was funded by the STFC grant ST/W001071/1. The work of A. P. Rouillard was funded by the ERC SLOW_SOURCE project (SLOW_SOURCE—DLV-819189). The work by T. D. Phan was supported by NASA grant 80NSSC20K1781 and NASA contract NNG04EB99C. We visualize data using the CLWeb software (http://clweb.irap.omp.eu/) developed by E. Penou; as well as the AMDA science analysis system (http://amda.cdpp.eu/) provided by the Centre de Données de la Physique des Plasmas (CDPP) supported by CNRS, CNES, Observatoire de Paris and Université Paul Sabatier (UPS), Toulouse. Finally, N. Fargette, B. Lavraud, T. D. Phan and C. J. Owen wish to acknowledge the support of the ISSI team lead by Denise Perrone and Sergio Toledo-Redondo, working on unravelling solar wind microphysics in the inner heliosphere.

References

Antiochos, S. K., Mikić, Z., Titov, V. S., Lionello, R., & Linker, J. A. 2011, ApJ, 731, 112
Bale, S. D., Badman, S. T., Bonnell, J. W., et al. 2019, Nature, 576, 237
Burlaga, L. F., & Ogilvie, K. W. 1970, ApJ, 159, 659
Cranmer, S. R. 2009, Liv. Rev. Sol. Phys., 6, 3
D'Amicis, R., & Bruno, R. 2015, ApJ, 805, 84
D'Amicis, R., Matteini, L., & Bruno, R. 2019, MNRAS, 483, 4665
D'Amicis, R., Bruno, R., Panasenco, O., et al. 2021, A&A, 656, A21
Davis, M. S., Phan, T. D., Gosling, J. T., & Skoug, R. M. 2006, Geophys. Rev. Lett., 33, L19102
de Hoffmann, F., & Teller, E. 1950, Phys. Rev., 80, 692
Eriksson, S., Gosling, J. T., Phan, T. D., et al. 2009, J. Geophys. Res. (Space Phys.), 114, A07103
Eriksson, S., Swisdak, M., Weygand, J. M., et al. 2022, ApJ, 933, 181
Gosling, J. T. 2007, ApJ, 671, L73
Gosling, J. T., & Szabo, A. 2008, J. Geophys. Res. (Space Phys.), 113, A10103
Gosling, J. T., Skoug, R. M., McComas, D. J., & Smith, C. W. 2005a, J. Geophys. Res. (Space Phys.), 110, A01107
Gosling, J. T., Skoug, R. M., McComas, D. J., & Smith, C. W. 2005b, Geophys. Rev. Lett, 32, L05105
Gosling, J. T., McComas, D. J., Skoug, R. M., & Smith, C. W. 2006, Geophys. Rev. Lett, 33, L17102
Gosling, J. T., Phan, T. D., Lin, R. P., & Szabo, A. 2007, Geophys. Rev. Lett, 34, L15110
Horbury, T. S., O'Brien, H., Carrasco Blazquez, I., et al. 2020, A&A, 642, A9
Hudson, P. D. 1970, Planet space sci., 18, 1611
Kasper, J. C., Bale, S. D., Belcher, J. W., et al. 2019, Nature, 576, 228
Klimchuk, J. A. 2006, Sol. Phys., 234, 41
Lapenta, G., & Knoll, D. A. 2005, ApJ, 624, 1049
Lavraud, B., Gosling, J. T., Rouillard, A. P., et al. 2009, Sol. Phys., 256, 379

Lavraud, B., Ruffenach, A., Rouillard, A. P., et al. 2014, J. Geophys. Res. (Space Phys.), 119, 26
Lavraud, B., Fargette, N., Réville, V., et al. 2020, ApJ, 894, L19
Lavraud, B., Kieokaew, R., Fargette, N., et al. 2021, A&A, 656, A37
Lopez, R. E., & Freeman, J. W. 1986, J. Geophys. Res., 91, 1701
Louarn, P., Fedorov, A., Prech, L., et al. 2021, A&A, 656, A36
Marsch, E., Rosenbauer, H., Schwenn, R., Muehlhaeuser, K. H., & Denskat, K. U. 1981, J. Geophys. Res., 86, 9199
Mistry, R., Eastwood, J. P., Phan, T. D., & Hietala, H. 2015, Geophys. Rev. Lett., 42(10), 513
Mistry, R., Eastwood, J. P., Phan, T. D., & Hietala, H. 2017, J. Geophys. Res. (Space Phys.), 122, 5895
Müller, D., St. Cyr, O. C., Zouganelis, I., , et al. 2020, A&A, 642, A1
Owen, C. J., Bruno, R., Livi, S., et al. 2020, A&A, 642, A16
Paschmann, G., Øieroset, M., & Phan, T. 2013, Space Sci. Rev., 178, 385
Phan, T. D., Gosling, J. T., Davis, M. S., et al. 2006, Nature, 439, 175
Phan, T. D., Gosling, J. T., & Davis, M. S. 2009, Geophys. Rev. Lett, 36, L09108
Phan, T. D., Gosling, J. T., Paschmann, G., et al. 2010, ApJ, 719, L199
Phan, T. D., Bale, S. D., Eastwood, J. P., et al. 2020, ApJS, 246, 34
Phan, T. D., Lavraud, B., Halekas, J. S., et al. 2021, A&A, 650, A13
Priest, E. R., Longcope, D. W., & Heyvaerts, J. 2005, ApJ, 624, 1057
Réville, V., Fargette, N., Rouillard, A. P., et al. 2022, A&A, 659, A110
Ruffenach, A., Lavraud, B., Owens, M. J., et al. 2012, J. Geophys. Res. (Space Phys.), 117, A09101
Ruffenach, A., Lavraud, B., Farrugia, C. J., et al. 2015, J. Geophys. Res. (Space Phys.), 120, 43
Sanchez-Diaz, E., Rouillard, A. P., Davies, J. A., et al. 2017, ApJ, 851, 32
Sanchez-Diaz, E., Rouillard, A. P., Lavraud, B., Kilpua, E., & Davies, J. A. 2019, ApJ, 882, 51
Sonnerup, B. U. O., Cahill, L. J., & J., 1967, J. Geophys. Res., 72, 171
Tilquin, H., Eastwood, J. P., & Phan, T. D. 2020, ApJ, 895, 68
Verscharen, D., Klein, K. G., & Maruca, B. A. 2019, Liv. Rev. Sol. Phys., 16, 5
Wang, Y. M. 1994, ApJ, 437, L67
Woodfield, E., Smith, A., Daggitt, T., & Turner, H. 2023, Astron. Geophys., 64, 3.30

Appendix A: Posterior ratio computation

In this Appendix, we detail how we compute a relevant equivalent to the posterior ratio.

Equation (5) states that the likelihood of the data follows a normal distribution of mean $\Delta\mathbf{V}_{\mathcal{M}}(t_i, \boldsymbol{\theta})$ and covariance matrix $\sigma_i^2 \mathbb{1}$ (4). In three dimensions, the Gaussian distribution writes:

$$\mathcal{G}(x, \mu, \Sigma) = \frac{1}{(2\pi)^{3/2}|\Sigma|^{1/2}} e^{-\frac{1}{2}(x-\mu)^{\mathrm{T}}\Sigma^{-1}(x-\mu)}, \tag{A.1}$$

with μ the mean vector, Σ the covariance matrix, and $|\Sigma|$ its determinant. By injecting this expression into Eq. (5), we may write

$$\begin{aligned} \mathrm{p}(\Delta\mathbf{V}(t_i) \mid t_i, \boldsymbol{\theta}) &= \mathcal{G}\left(\Delta\mathbf{V}(t_i),\ \Delta\mathbf{V}_{\mathcal{M}}(t_i, \boldsymbol{\theta}),\ \sigma_i^2 \mathbb{1}\right) \\ &= \frac{1}{(2\pi\sigma_i^2)^{3/2}} e^{-\frac{1}{2\sigma_i^2}|\Delta\mathbf{V}(t_i) - \Delta\mathbf{V}_{\mathcal{M}}(t_i, \boldsymbol{\theta})|^2}. \end{aligned} \tag{A.2}$$

We then assume independent measurements, which means that $\mathrm{p}(\Delta\mathbf{V} \mid t, \boldsymbol{\theta}) = \prod_i \mathrm{p}(\Delta\mathbf{V}(t_i) \mid t_i, \boldsymbol{\theta})$, and, by taking the logarithm of this expression, the log-likelihood of the data writes

$$\begin{aligned} \ln\left(\mathrm{p}(\Delta\mathbf{V} \mid \widehat{t}, \boldsymbol{\theta})\right) &= \sum_{i=1}^{N} \ln \mathrm{p}(\Delta\mathbf{V}(t_i) \mid t_i, \boldsymbol{\theta}) \\ &= \sum_{i=1}^{N} -\frac{1}{2\sigma_i^2}|\Delta\mathbf{V}(t_i) - \Delta\mathbf{V}_{\mathcal{M}}(t_i, \boldsymbol{\theta})|^2 - \frac{3}{2}\ln(2\pi\sigma_i^2) \end{aligned}. \tag{A.3}$$

We may then compute the posterior probability for each model through the Bayes equation (eq. (7)) and compute the posterior ratio:

$$\frac{p\left(\text{jet}|\, \widehat{t}, \Delta\mathbf{V}\right)}{p\left(\text{no jet}|\, \widehat{t}, \Delta\mathbf{V}\right)} = \frac{\sum_{k=3,4} p(\boldsymbol{\theta}_k|\, \widehat{t}, \Delta\mathbf{V})}{\sum_{k=1,2} p(\boldsymbol{\theta}_k|\, \widehat{t}, \Delta\mathbf{V})}. \tag{A.4}$$

Here, the notation 'jet $\mid \widehat{t} = \theta_3 \bigcup \theta_4 \mid \widehat{t}$', designates the random variable associated to the event 'the points in the time window $\widehat{t}$ are part of a reconnection jet'.

As described in Sect. 3.1, this event can occur in one of two ways: a correlated/anticorrelated or an anticorrelated/correlated reconnection exhaust (i.e. θ_3 or θ_4). On the other hand, the complement of this event, (i.e. $\theta_1 \bigcup \theta_2 \mid \widehat{t}$), is denoted 'no jet = $\overline{\text{jet}}$'.

For each model, the posterior probability can be rewritten as

$$p(\boldsymbol{\theta}_k|\, \widehat{t}, \Delta\mathbf{V}) = \frac{p(\boldsymbol{\theta}_k|\, \widehat{t}) p(\Delta\mathbf{V}|\, \widehat{t}, \boldsymbol{\theta}_k)}{p(\Delta\mathbf{V}|\, \widehat{t})}. \tag{A.5}$$

For symmetry considerations, we must have $p(\boldsymbol{\theta}_3|\, \widehat{t}) = p(\boldsymbol{\theta}_4|\, \widehat{t}) = p(\text{jet}|\, \widehat{t})/2$ a priori, because a correlated/anti-correlated reconnection jet is nothing more than an anti-correlated/correlated reconnection jet through time reversal. We can also consider that $p(\boldsymbol{\theta}_1|\, \widehat{t}) = p(\boldsymbol{\theta}_2|\, \widehat{t}) = p(\text{no jet}|\, \widehat{t})/2$, because the probability of observing either a correlated or an anti-correlated solar wind relates to being in one or the other magnetic hemisphere. Moreover, the events 'jet' and 'no jet' are complements for a given window size N, such that $p(\text{no jet}|\, \widehat{t}) = 1 - p(\text{jet}|\, \widehat{t})$. Equation (A.4) can therefore be developed as

$$\frac{p\left(\text{jet}|\, \widehat{t}, \Delta\mathbf{V}\right)}{p\left(\text{no jet}|\, \widehat{t}, \Delta\mathbf{V}\right)} = \left(\frac{p(\text{jet}|\, \widehat{t})}{1 - p(\text{jet}|\, \widehat{t})}\right) \frac{\sum_{k=3,4} p(\Delta\mathbf{V}|\, \widehat{t}, \boldsymbol{\theta}_k)}{\sum_{k=1,2} p(\Delta\mathbf{V}|\, \widehat{t}, \boldsymbol{\theta}_k)}. \tag{A.6}$$

As it is likely that this ratio will get exponentially small with N, it is convenient (to compare values between window sizes as well as for numerical reasons) to define a normalised posterior ratio $Q(\widehat{t})$ such that

$$Q(\widehat{t}) = \left(\frac{p\left(\text{jet}|\, \widehat{t}, \Delta\mathbf{V}\right)}{p\left(\text{no jet}|\, \widehat{t}, \Delta\mathbf{V}\right)}\right)^{1/N}. \tag{A.7}$$

The idea behind this expression is that $Q(\widehat{t})$ would represent the posterior ratio of a single point if both posteriors could be expressed as the product of independent probabilities (which they generally cannot). In our case, this normalised ratio can be thought of as an average over a given time window $\widehat{t}$. This way, one can expect to get rid of most of the window's size dependence in the posterior ratio by using $Q(\widehat{t})$.

To simplify its expression, we may note that $p(\text{jet}|\, \widehat{t}) \lll 1$ in general. Indeed, if we write $p(\text{jet}|\, \widehat{t})$ as $\prod_{i=1}^{N} p(\text{jet}|\, t_i)$ with $p(\text{jet}|\, t_i) \sim 0.01$, as we assumed in the main part, $p(\text{jet}|\, \widehat{t})$ would then be inferior to the numerical error for $N > 8$. Therefore, we express $Q(\widehat{t})$ as

$$Q(\widehat{t}) = p(\text{jet}|\, \widehat{t})^{\frac{1}{N}} \left(\frac{\sum_{k=3,4} p(\Delta\mathbf{V}|\, \widehat{t}, \boldsymbol{\theta}_k)}{\sum_{k=1,2} p(\Delta\mathbf{V}|\, \widehat{t}, \boldsymbol{\theta}_k)}\right)^{1/N}. \tag{A.8}$$

Looking at the second part of the expression now, we note that we are still summing probabilities, and therefore cannot avoid considering their actual value rather than taking their logarithm. However, the $p(\Delta\mathbf{V}|\, \boldsymbol{\theta}_k, \widehat{t})$ terms are often too small to compute (as we are multiplying N values below 1) and it would be more convenient to simplify this expression and only consider 'normalised' probabilities $p(\Delta\mathbf{V}|\, \boldsymbol{\theta}_k, \widehat{t})^{1/N}$. We therefore proposed the following approximation:

$$Q(\widehat{t}) \simeq p(\text{jet}|\, \widehat{t})^{\frac{1}{N}} \frac{\sum_{k=3,4} p(\Delta\mathbf{V}|\, \widehat{t}, \boldsymbol{\theta}_k)^{\frac{1}{N}}}{\sum_{k=1,2} p(\Delta\mathbf{V}|\, \widehat{t}, \boldsymbol{\theta}_k)^{\frac{1}{N}}}. \tag{A.9}$$

We can note that one term will always dominate the others either in the numerator or the denominator. The reason is that if for example the parameter set $\boldsymbol{\theta}_1$ were found to properly describe the data, then the set $\boldsymbol{\theta}_2$ would cause the model to predict a completely anticorrelated data set, thus making its likelihood, $p(\Delta\mathbf{V}|\, \widehat{t}, \boldsymbol{\theta}_2)$, very low. In such a case, the approximation

$$\left(\sum_k p(\Delta\mathbf{V}|\, \widehat{t}, \boldsymbol{\theta}_k)\right)^{1/N} \sim \sum_k p(\Delta\mathbf{V}|\, \widehat{t}, \boldsymbol{\theta}_k)^{\frac{1}{N}} \tag{A.10}$$

makes at most a relative error of order

$$\varepsilon = \frac{1}{N} \frac{\min_k p(\Delta\mathbf{V}|\, \widehat{t}, \boldsymbol{\theta}_k)}{\max_k p(\Delta\mathbf{V}|\, \widehat{t}, \boldsymbol{\theta}_k)} \ll 1. \tag{A.11}$$

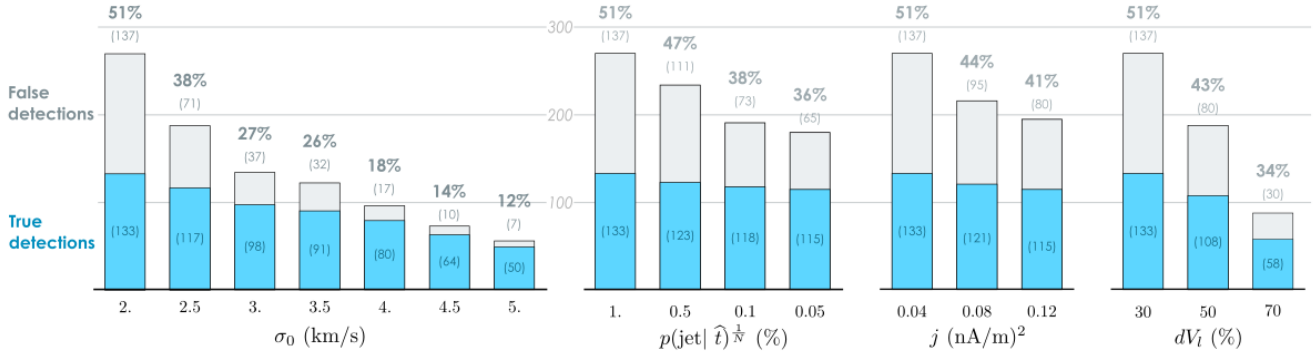

Fig. A.1. Variation of the number of detections depending on the input parameter values. Among the detections, the grey bars indicate false detections while the blue bars are true-positive detections. The background grid (horizontal grey lines) is to guide the eye for the total number of detections (true and false). The FP rate is also written at the top of each bar.

However, both terms can be of the same order on the other side of the fraction, the error being maximised when $p(\Delta\mathbf{V}|\,\widehat{t},\boldsymbol{\theta}_1) = p(\Delta\mathbf{V}|\,\widehat{t},\boldsymbol{\theta}_2)$ (or respectively $p(\Delta\mathbf{V}|\,\widehat{t},\boldsymbol{\theta}_3) = p(\Delta\mathbf{V}|\,\widehat{t},\boldsymbol{\theta}_4)$). In the latter case, the relative error is

$$\varepsilon = 2^{\frac{1}{N}-1} \sim 1, \tag{A.12}$$

and is therefore non-negligible. We note that this situation is not problematic if $p(\Delta\mathbf{V}|\,\widehat{t},\boldsymbol{\theta}_{\{1,2\}}) \ll p(\Delta\mathbf{V}|\,\widehat{t},\boldsymbol{\theta}_{\{2,1\}})$ and $p(\Delta\mathbf{V}|\,\widehat{t},\boldsymbol{\theta}_3) \sim p(\Delta\mathbf{V}|\,\widehat{t},\boldsymbol{\theta}_4)$, because it would lead to a small value of $Q(\widehat{t})$ with or without the approximation and thus have no impact on the jet detections. The only situation where the approximation can have an impact is if $p(\Delta\mathbf{V}|\,\widehat{t},\boldsymbol{\theta}_{\{3,4\}}) \ll p(\Delta\mathbf{V}|\,\widehat{t},\boldsymbol{\theta}_{\{4,3\}})$ and $p(\Delta\mathbf{V}|\,\widehat{t},\boldsymbol{\theta}_1) \sim p(\Delta\mathbf{V}|\,\widehat{t},\boldsymbol{\theta}_2)$, where the Eq. (A.9) underestimates the actual value of $Q(\widehat{t})$ by a factor of up to 2. We also note that this should not cause any false detections because it is an underestimation of the actual ratio, but might cause us to miss jets that are very close to the threshold. However, this effect should remain marginal because it consists at most in an additional constant $-\ln(2) \simeq -0.7$ in $\ln Q(\widehat{t})$, to be compared with the axis scale of Fig. 2.

Appendix B: Algorithm performance

In this section, we analyse how the algorithm performs when we vary its different input parameters. In Fig. A.1, we show how the number of detections and FP rate evolve depending on these parameter values. We see that the number of detections and FP rate drop rapidly when we increase σ_0, the assumed noise on the PAS data. If one wishes to adopt a conservative approach, increasing σ_0 is the best way to achieve a low FP rate. By contrast, decreasing $p(\text{jet}|\,\widehat{t})^{\frac{1}{N}}$ or increasing j seem to decrease the FP rate without significantly affecting the detection number. Therefore, these last two parameters might be better fine tuned in the future to reach an optimum in both the number of detections and FP rate. Finally, increasing the constraint on the magnitude of the jet decreases the number of detections and FP rate, as should be expected.

Appendix C: Data gaps

Table C.1. Timetable of data gaps

#	Start time	End time
1	2020-07-15 06:00	2020-07-15 16:30
2	2020-07-16 01:00	2020-07-16 05:30
3	2020-07-18 03:40	2020-07-20 05:00
4	2020-07-22 05:30	2020-07-22 11:30
5	2020-07-23 14:00	2020-07-24 01:30
6	2020-07-24 22:30	2020-07-26 00:30
7	2020-07-25 11:55	2020-07-25 16:31
8	2020-07-26 18:00	2020-07-27 04:33
9	2020-07-27 07:00	2020-07-27 11:00
10	2020-08-01 11:28	2020-08-01 16:09
11	2020-08-02 16:00	2020-08-02 23:00
12	2020-08-02 23:52	2020-08-03 04:43
13	2020-08-05 03:00	2020-08-05 09:00
14	2020-08-06 00:00	2020-08-08 17:00
15	2020-08-10 00:00	2020-08-10 04:30
16	2020-08-10 07:50	2020-08-11 03:38

Appendix D: Jet timetable

Table D.1. Timetable of reconnection exhausts

#	Date	Start time	End time
1	2020-07-14	05:36:10	05:36:51
2	2020-07-14	08:14:19	08:15:07
3	2020-07-14	08:39:11	08:39:44
4	2020-07-14	09:35:43	09:36:15
5	2020-07-14	10:42:39	10:43:11
6	2020-07-14	10:45:15	10:47:03
7	2020-07-14	11:05:47	11:07:31
8	**2020-07-14**	**12:01:35**	**12:02:07**
9	2020-07-14	20:02:20	20:02:44
10	2020-07-15	03:09:12	03:10:04
11	2020-07-15	20:01:44	20:02:23
12	2020-07-16	06:56:43	06:57:20
13	2020-07-16	12:34:30	12:38:10
14	2020-07-16	14:27:52	14:28:32
15	**2020-07-16**	**14:56:20**	**14:56:44**
16	2020-07-16	18:28:08	18:42:48
17	2020-07-16	21:21:19	21:21:48
18	2020-07-16	21:56:40	21:57:00
19	**2020-07-16**	**22:01:42**	**22:02:15**
20	2020-07-16	23:01:00	23:02:04
21	**2020-07-17**	**20:58:10**	**20:58:40**
22	2020-07-20	08:10:40	08:17:20
23	2020-07-20	10:31:04	10:33:36
24	2020-07-20	11:28:50	11:30:20
25	2020-07-20	22:41:12	22:43:00
26	2020-07-21	00:44:45	00:46:36
27	2020-07-21	03:24:45	03:25:27
28	2020-07-21	08:33:04	08:33:48
29	2020-07-21	10:08:12	10:09:12
30	2020-07-21	11:04:43	11:05:07
31	2020-07-21	15:17:40	15:22:00
32	2020-07-21	15:51:52	15:52:24
33	2020-07-21	16:05:16	16:05:48
34	2020-07-21	20:40:36	20:43:52
35	2020-07-21	22:06:24	22:07:16
36	2020-07-21	22:49:20	22:49:47
37	2020-07-22	04:20:10	04:22:15
38	2020-07-22	04:35:39	04:36:43
39	**2020-07-22**	**16:01:20**	**16:01:57**
40	2020-07-22	16:04:00	16:04:29
41	2020-07-22	19:03:11	19:03:30
42	2020-07-22	23:09:37	23:10:13
43	2020-07-23	07:50:00	07:51:09
44	2020-07-23	07:55:28	07:56:38
45	2020-07-23	07:59:59	08:05:27
46	2020-07-23	08:05:39	08:07:37
47	2020-07-23	08:13:42	08:17:20
48	2020-07-23	08:45:35	08:47:21
49	2020-07-23	09:20:00	09:21:00
50	2020-07-23	10:02:36	10:02:51
51	2020-07-23	12:12:21	12:13:17
52	2020-07-23	12:51:09	12:51:50
53	2020-07-23	13:12:33	13:13:21
54	2020-07-23	13:40:00	13:41:06
55	2020-07-23	13:52:36	13:53:18
56	2020-07-23	13:55:21	13:55:57
57	2020-07-24	01:30:30	01:38:00
58	2020-07-24	02:24:00	02:29:16
59	2020-07-24	06:27:41	06:31:41
60	2020-07-24	07:41:53	07:42:45
61	2020-07-24	18:34:19	18:35:35
62	2020-07-24	18:49:23	18:50:11
63	2020-07-24	21:32:55	21:34:25
64	2020-07-25	02:11:09	02:12:34
65	2020-07-25	08:46:51	08:47:39
66	**2020-07-25**	**09:33:20**	**09:33:38**
67	2020-07-25	23:30:12	23:31:49
68	2020-07-26	01:55:54	01:56:18
69	2020-07-26	05:57:15	05:57:55
70	2020-07-27	23:28:47	23:30:39
71	2020-07-28	01:16:53	01:21:10
72	2020-07-28	01:26:34	01:28:17
73	2020-07-28	01:53:21	01:53:40
74	2020-07-28	03:42:53	03:43:35
75	2020-07-28	05:03:37	05:06:25
76	2020-07-28	19:10:49	19:11:21
77	2020-07-29	01:38:21	01:39:03
78	2020-07-29	14:35:21	14:36:19
79	2020-07-29	14:35:25	14:36:30
80	2020-07-29	18:02:50	18:03:18

Table D.1. continued.

Table D.1. continued.

#	Date	Start time	End time
81	2020-07-29	20:53:13	20:53:48
82	**2020-07-29**	**22:11:46**	**22:12:42**
83	2020-07-29	22:14:11	22:15:10
84	2020-07-29	23:33:36	23:34:36
85	2020-07-30	00:43:55	00:44:42
86	2020-07-30	04:29:18	04:30:30
87	2020-07-30	05:55:14	05:56:22
88	2020-07-30	10:12:58	10:13:42
89	2020-07-30	10:40:19	10:41:07
90	2020-07-30	17:23:38	17:27:38
91	2020-07-30	18:25:22	18:25:52
92	2020-07-30	21:45:50	21:47:18
93	2020-07-31	03:17:25	03:18:10
94	2020-07-31	04:14:41	04:14:58
95	2020-07-31	07:53:13	07:55:42
96	2020-07-31	08:09:35	08:13:00
97	2020-07-31	09:56:18	09:58:18
98	2020-07-31	10:00:05	10:01:09
99	2020-07-31	11:13:26	11:15:06
100	2020-07-31	22:57:45	22:58:07
101	2020-07-31	23:19:27	23:19:59
102	2020-08-01	02:29:57	02:30:35
103	**2020-08-01**	**06:02:38**	**06:05:36**
104	2020-08-01	16:52:10	16:53:02
105	2020-08-02	00:33:06	00:34:02
106	2020-08-03	17:23:58	17:24:34
107	2020-08-03	19:09:02	19:09:43
108	2020-08-03	23:46:16	23:48:00
109	2020-08-04	01:34:10	01:35:30
110	2020-08-04	14:08:02	14:08:31
111	2020-08-04	19:51:58	19:52:54
112	2020-08-04	21:16:00	21:16:38
113	2020-08-05	01:20:22	01:20:46
114	2020-08-05	10:08:20	10:09:43
115	2020-08-05	10:49:23	10:49:47
116	2020-08-05	11:34:00	11:37:45
117	2020-08-05	18:44:48	18:45:51
118	2020-08-05	18:51:30	18:53:00
119	2020-08-05	20:22:54	20:23:44
120	**2020-08-05**	**20:35:23**	**20:36:47**
121	2020-08-08	17:11:41	17:18:45
122	2020-08-08	18:19:37	18:22:00
123	2020-08-08	19:49:07	19:49:59
124	**2020-08-09**	**01:12:22**	**01:13:41**
125	**2020-08-09**	**01:17:30**	**01:18:15**
126	2020-08-09	11:56:43	11:59:30
127	2020-08-09	22:28:35	22:29:07
128	2020-08-11	03:57:03	03:57:58
129	2020-08-11	11:19:19	11:19:43
130	**2020-08-11**	**13:48:33**	**13:48:46**
131	**2020-08-11**	**13:53:11**	**13:53:35**
132	2020-08-11	15:20:06	15:20:20
133	2020-08-11	15:49:45	15:50:35
134	2020-08-11	16:53:31	16:54:55
135	2020-08-11	17:08:20	17:10:00
136	2020-08-11	17:17:50	17:18:09
137	2020-08-11	18:22:03	18:23:27
138	2020-08-11	19:43:03	19:43:27
139	2020-08-11	20:10:59	20:11:23
140	2020-08-11	20:49:04	20:49:31
141	2020-08-11	20:57:07	20:57:25
142	2020-08-11	23:11:47	23:12:27
143	2020-08-12	04:59:27	04:59:51
144	2020-08-12	07:22:00	07:26:49
145	2020-08-12	09:02:32	09:02:56
146	2020-08-12	09:09:56	09:11:16

Notes. Reconnection exhausts detected between July 14, 2020, at 05:15 and August 13, 2020, at 00:00. Bold lines highlight the nine reconnection exhausts that were not detected by the algorithm.